Ferromagnetic $Ge_{1-x}M_x$ (M = Mn, Fe, and Co) Nanowires

Yong Jae Cho, Chang Hyun Kim, Han Sung Kim, Wang Su Lee, Seong-Hun Park, and Jeunghee Park*

Department of Chemistry, Korea University, Jochiwon, Chungnam 339-700, Korea

Seung Yong Bae

Chemical R&D Center, Samsung Cheil Industry Incorporated, Uiwang 437-711, Korea

Bongsoo Kim

Department of Chemistry, KAIST, Daejeon 305-701, Korea

Hangil Lee and Jae-Young Kim

Pohang Accelerator Laboratory, POSTECH, Pohang 790-784, Korea

Received December 13, 2007. Revised Manuscript Received May 1, 2008

We synthesized Ge and $Ge_{1-x}M_x$ (M = Mn, Co, and Fe, $x \leq 0.4$) nanowires using the thermal vapor transport method. All of the nanowires consisted of single-crystalline Ge nanocrystals grown uniformly with the [111] direction. High-resolution X-ray diffraction showed no metal cluster formation for any of the $Ge_{1-x}M_x$ nanowires, and the reduction of the lattice constant for the Mn-substituted nanowires. X-ray absorption spectroscopy and X-ray magnetic circular dichroism measurements revealed that the Mn^{2+} ions preferentially occupy the tetrahedral sites, substituting for Ge. The magnetic moment of the Mn ions reaches a maximum for $x = 0.1$, which is much larger than that of the Fe or Co ions. The magnetic hysteresis confirms the room-temperature ferromagnetism of the $Ge_{1-x}Mn_x$ nanowires, which is also maximized at $x = 0.1$. We suggest that the Mn ions produce dopant−acceptor hybridization with host defects in the p-type Ge nanowires. The Mn substitution is more effective to form significant ferromagnetic Ge nanowires, compared to the Fe or Co substitution.

1. Introduction

Dilute magnetic semiconductors (DMSs) that are obtained by doping semiconductor materials with magnetic impurities have been investigated extensively due to their potential application in spintronic devices.[1] Among the various types of DMSs, Ge-based DMSs have recently attracted special attention, due mainly to their potential integration with conventional Si-based electronic devices. Theoretical calculations, using the Zener model based on mean-field theory, predicted the stabilization of the ferromagnetic ordering at a sufficiently high concentration ($3.5 \times 10^{20}/cm^3$) of hole carriers and the Curie temperature (T_C) of the p-type $Ge_{0.95}Mn_{0.05}$ to be 80 K.[2] Other theoretical calculations also predicted that the ferromagnetic stabilization is dominated by Ruderman−Kittel−Kasuya−Yosida-like interactions or double-exchange interactions via localized holes.[3–5] Previous intensive experimental studies of $Ge_{1-x}Mn_x$ single crystals and nanocrystalline thin films reported a wide range of T_C values from 25 to 300 K, which support their high-T_C ferromagnetism.[6–15] However, a number of research groups suggested that their ferromagnetism is due to secondary phases (e.g., Ge_8Mn_{11} or Ge_3Mn_5 alloys).[10–15] Despite the confusion surrounding the origin of their ferromagnetism, $Ge_{1-x}Mn_x$ DMSs are still very promising materials for spintronic devices operating at high temperature.

On the other hand, there have only been a few studies of Ge-based DMSs using other transition metal dopants such as Fe and Co.[16–18] The $T_C = 233$ K was reported for 5% Fe, and $T_C = 150$ K for 2% Co doping.[16,17] It has also been suggested that secondary phases such as Ge_2Fe_3 are respon-

* Author to whom correspondence should be addressed. E-mail: parkjh@korea.ac.kr.

(1) (a) Wolf, S. A.; Awschalom, D. D.; Buhrman, R. A.; Daughton, J. M.; von Molnár, S.; Roukes, M. L.; Chtchelkanova, A. Y.; Treger, D. M. *Science* **2001**, *294*, 1488. (b) Ohno, H. *Science* **1998**, *281*, 951.
(2) (a) Dietl, T.; Ohno, H.; Matsukura, F.; Cibert, J.; Ferrand, D. *Science* **2000**, *287*, 1019. (b) Dietl, T.; Ohno, H.; Matsukura, F. *Phys. Rev. B* **2001**, *63*, 195205.
(3) Zhao, Y.-J.; Shishidou, T.; Freeman, A. J. *Phys. Rev. Lett.* **2003**, *90*, 047204.
(4) Weng, H.; Dong, J. *Phys. Rev. B* **2005**, *71*, 035201.
(5) Huang, X.; Makmal, A.; Chelikowsky, J. R.; Kronik, L. *Phys. Rev. Lett.* **2005**, *94*, 236801.
(6) Park, Y. D.; Hanbicki, A. T.; Erwin, S. C.; Hellberg, C. S.; Sullivan, J. M.; Mattson, J. E.; Ambrose, T. F.; Wilson, A.; Spanos, G.; Jonker, B. T. *Science* **2002**, *295*, 651.
(7) Cho, S.; Choi, S.; Hong, S. C.; Kim, Y.; Ketterson, J. B.; Kim, B.-J.; Kim, Y. C.; Jung, J.-H. *Phys. Rev. B* **2002**, *66*, 033303.
(8) (a) Tsui, F.; He, L.; Ma, L.; Tkachuk, A.; Chu, Y. S.; Nakajima, K.; Chikyow, T. *Phys. Rev. Lett.* **2003**, *91*, 177203. (b) Tsui, F.; He, L.; Tkachuk, A.; Vogt, S.; Chu, Y. S. *Phys. Rev. B* **2004**, *69*, 081304 (R)
(9) (a) Zeng, C.; Erwin, S. C.; Feldman, L. C.; Li, A. P.; Jin, R.; Song, Y.; Thompson, J. R.; Weitering, H. H. *Appl. Phys. Lett.* **2003**, *83*, 5002. (b) Li, A. P.; Wendelken, J. F.; Shen, J.; Feldman, L. C.; Thompson, J. R.; Weitering, H. H. *Phys. Rev. B* **2005**, *72*, 195205. (c) Li, A. P.; Zeng, C.; van Benthem, K.; Chisholm, M. F.; Shen, J.; Nageswara Rao, S. V. S.; Dixit, S. K.; Feldman, L. C.; Petukhov, A. G.; Foygel, M.; Weitering, H. H. *Phys. Rev. B* **2007**, *75*, 201201.

10.1021/cm7035635 CCC: $40.75
Published on Web 06/26/2008

sible for their ferromagnetism.[18] Recently, theoretical calculations were performed for the ferromagnetism of the entire first-period transition metals, which showed Fe and Co to be far less efficient than Mn in promoting ferromagnetic alignment and a high magnetic moment.[19] Therefore, extended studies of doping with various transition metals would help to obtain a better comprehension of the physical mechanism determining the magnetic ordering temperature and possibly lead to the discovery of even more promising compounds.

Since the discovery of carbon nanotubes, intensive research activities have been directed toward one-dimensional (1D) nanostructures, which are considered to be well-defined building blocks for the construction of various nanoscale devices.[20] As regard transition metal-doped Ge nanowires (NWs), however, such examples are rather scarce in the literature. Room-temperature ferromagnetic $Ge_{1-x}Mn_x$ ($x \leq 0.05$) NWs were synthesized within the pores of an anodized aluminum oxide membrane using a supercritical fluid inclusion-phase technique.[21] High-T_C (>400 K) ferromagnetic Mn-rich Ge (Ge_2Mn alloy) nanocolumns were grown by the molecular beam epitaxy method.[22] Recent calculations on Mn-doped Ge NWs showed that the Mn impurities introduce a local magnetic moment due to d levels resonant with the valence band.[23] To the best of our knowledge, however, there have been no previous reports on Ge NWs with Fe or Co doping. Moreover, it is significant to elucidate the electronic structures which are responsible for their magnetic properties. However, the correlations between their electronic structures and magnetic moments are far from being carefully examined for well-defined nanowire structures.

Herein, we report the synthesis of single-crystalline $Ge_{1-x}M_x$ (M = Mn, Fe, and Co, $x \leq 0.4$) NWs, Ge, $Ge_{0.95}Mn_{0.05}$, $Ge_{0.9}Mn_{0.1}$, $Ge_{0.8}Mn_{0.2}$, $Ge_{0.9}Fe_{0.1}$, $Ge_{0.9}Co_{0.1}$, and $Ge_{0.6}Co_{0.4}$ NWs, by the vapor transport method. The metal substituent was homogeneously distributed along the whole nanowires, with a controlled concentration. These well-defined single-crystalline 1D nanostructures (with no cluster formation) make it possible to scrutinize the magnetic properties and electronic structures of DMS materials depending on the nature of metal dopant and its concentration. The lattice constants and electronic structures were thoroughly investigated by high-resolution X-ray diffraction (XRD), Raman spectroscopy, X-ray photoelectron spectroscopy (XPS), X-ray absorption spectroscopy (XAS), and X-ray magnetic circular dichroism (XMCD). All of the nanowires exhibited ferromagnetic behaviors at room temperature, but their magnetic moment depends strongly on the properties of the metal dopant. We found a remarkable correlation of the ferromagnetic properties with their electronic structures and discussed the origin of their ferromagnetism.

2. Experimental Section

Ge (99.98%, Aldrich) powder and $MnCl_2$ (99%, Aldrich) (or $CoCl_2$ (99%, Aldrich) or $FeCl_2$ (99%, Aldrich)) beads were placed separately inside a quartz tube reactor. A silicon substrate on which a Au thin film (5 nm thick) was deposited was positioned at a distance of 10 cm away from the Ge source. Argon was allowed to flow at a rate of 500 sccm while raising or lowering the temperature. The metal source was evaporated at temperature in the range of 700−800 °C, and the Ge powder was evaporated at 900 °C using a separate heating stage, for 1 h under argon flow. The temperature of the substrate was approximately 800 °C. Higher evaporation temperature of the metal source increases the metal contents of the Ge NWs. The undoped Ge NWs were synthesized using the evaporation of only Ge powder under the same conditions.

The products were analyzed by scanning electron microscopy (SEM, Hitachi S-4700), field emission transmission electron microscopy (TEM, Jeol JEM 2100F and FEI TECNAI G^2 200 kV), high-voltage TEM (HVEM, Jeol JEM ARM 1300S, 1.25 MV), field emission TEM (FEI TECNAI G^2 200 kV), and energy-dispersive X-ray fluorescence spectroscopy (EDX). Raman spectroscopy (Horiba Jobin-Yvon HR-800 UV) was performed using the 514.5 nm line of an argon ion laser. High-resolution XRD patterns were obtained using the 8C2 beam line of the Pohang Light Source (PLS) with monochromatic radiation (λ = 1.54520 Å). XPS was performed using the 8A1 beam line of the PLS and a laboratory-based spectrometer (ESCALAB 250, VG Scientifics) using a photon energy of 1486.6 eV (Al Kα).

The XAS and XMCD measurements were carried out at the PLS elliptically polarized undulator beam line, 2A. The samples were introduced into an experimental chamber with a base pressure of 5×10^{-10} Torr. The spectra were collected in the total electron yield (TEY) mode. A 0.1 T electromagnet was used to switch the magnetization direction. The magnetization direction was flipped between the parallel (ρ^+) and antiparallel (ρ^-) directions with respect to the photon helicity vector for each data point. The degree of circular polarization (95%) of the incident light was taken into

(10) (a) Gunnella, R.; Morresi, L.; Pinto, N.; Murri, R.; Ottaviano, L.; Passacantando, M.; D'Ozario, F.; Lucari, F. *Surf. Sci.* **2005**, *577*, 22. (b) Ottaviano, L.; Passacantando, M.; Picozzi, S.; Continenza, A.; Gunnella, R.; Verna, A.; Bihlmayer, G.; Impellizzeri, G.; Priolo, F. *Appl. Phys. Lett.* **2006**, *88*, 061907. (c) Passacantando, M.; Ottaviano, L.; D'Ozario, F.; Lucari, F.; De Biase, M.; Impellizzeri, G.; Priolo, F. *Phys. Rev. B* **2006**, *73*, 195207. (d) Ottaviano, L.; Parisse, P.; Passacantando, M.; Picozzi, S.; Verna, A.; Impellizzeri, G.; Priolo, F. *Surf. Sci.* **2006**, *600*, 4723.
(11) Cho, Y. M.; Yu, S. S.; Ihm, Y. E.; Kim, D.; Kim, H.; Baek, J. S.; Kim, C. S.; Lee, B. T. *J. Magn. Magn. Mater.* **2004**, *282*, 385.
(12) Kang, J.-S.; Kim, G.; Wi, S. C.; Lee, S. S.; Choi, S.; Cho, S.; Han, S. W.; Kim, K. H.; Song, H. J.; Shin, H. J.; Sekiyama, A.; Kasai, S.; Suga, S.; Min, B. I. *Phys. Rev. Lett.* **2005**, *94*, 147202.
(13) Sugahara, S.; Lee, K. L.; Yada, S.; Tanaka, M. *Jpn. J. Appl. Phys.* **2005**, *44*, L1426.
(14) Jaeger, C.; Bihler, C.; Vallaitis, T.; Goennenwein, S. T. B.; Opel, M.; Gross, R.; Brandt, M. S. *Phys. Rev. B* **2006**, *74*, 045330.
(15) Li, H.; Wu, Y.; Guo, Z.; Luo, P.; Wang, S. *J. Appl. Phys.* **2006**, *100*, 103908.
(16) Choi, S.; Hong, S. C.; Cho, S.; Kim, Y.; Ketterson, J. B.; Jung, C.-U.; Rhie, K.; Kim, B.-J.; Kim, Y. C. *J. Appl. Phys.* **2003**, *93*, 7670.
(17) Ko, V.; Teo, K. L.; Liew, T.; Chong, T. C. *Appl. Phys. Lett.* **2006**, *89*, 042504.
(18) Goswami, R.; Kioseoglou, G.; Hanbicki, A. T.; van'tErve, O. M. J.; Jonker, B. T.; Spanos, G. *Appl. Phys. Lett.* **2005**, *86*, 032509.
(19) Continenza, A.; Profeta, G.; Picozzi, S. *Phys. Rev. B* **2006**, *73*, 035212.
(20) (a) Hu, J.; Odom, T. W.; Lieber, C. M. *Acc. Chem. Res.* **1999**, *32*, 435. (b) Gudiksen, M. S.; Lauhon, L. J.; Wang, J.; Smith, D. C.; Lieber, C. M. *Nature (London)* **2002**, *415*, 617. (c) Duan, X.; Huang, Y.; Agarwal, R.; Lieber, C. M. *Nature (London)* **2003**, *421*, 241.
(21) (a) Kulkarni, J. S.; Kazakova, O.; Erts, D.; Morris, M. A.; Shaw, M. T.; Holmes, J. D. *Chem. Mater.* **2005**, *17*, 3615. (b) Kazakova, O.; Kulkarni, J. S.; Holmes, J. D.; Demokritov, S. O. *Phys. Rev. B* **2005**, *72*, 094415. (c) Kazakova, O.; Kulkarni, J. S.; Arnold, D. C.; Holmes, J. D. *J. Appl. Phys.* **2007**, *101*, 09H108.
(22) Jamet, M.; Barski, A.; Devillers, T.; Poydenot, V.; Dujardin, R.; Bayle-Guillemaud, P.; Rohtman, J.; Bellet-Almaric, E.; Marty, A.; Cibert, J.; Mattana, R.; Tatarenko, S. *Nat. Mater.* **2006**, *5*, 653.
(23) Arantes, J. T.; da Silva, J. R. A.; Fazzio, A. *Phys. Rev. B* **2007**, *75*, 115113.

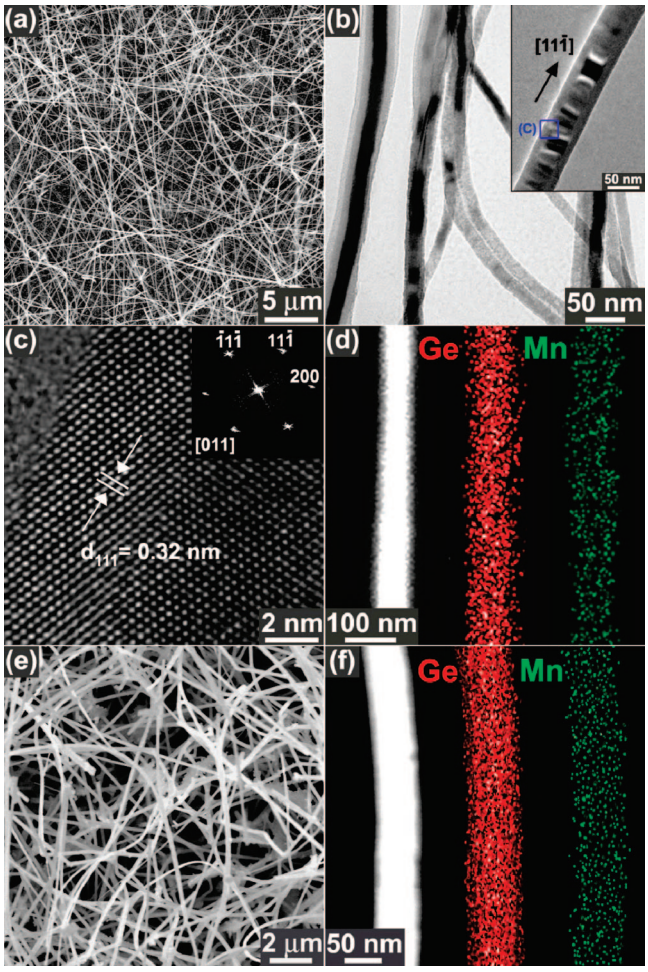

Figure 1. (a) SEM images of the $Ge_{0.9}Mn_{0.1}$ NWs grown on the substrates. (b) The TEM image shows the general morphology of the $Ge_{0.9}Mn_{0.1}$ NWs. The average diameter is 60 nm. (c) Lattice-resolved TEM images of a selected nanowire (whose larger-scaled TEM image is shown in the inset of (b)) and its corresponding FFT ED pattern (inset), revealing the single-crystalline Ge nanocrystals grown along the [111] direction. (d) EDX elemental mapping revealing that the nanowires are homogeneously composed of Ge and Mn. The STEM image is shown on the left. (e) SEM images of the $Ge_{0.8}Mn_{0.2}$ NWs and (f) their STEM image and EDX elemental mapping. The 20% Mn element is distributed homogeneously over the whole NWs.

account in the spectra. The magnetic properties were studied using a superconducting quantum interference device (SQUID, Quantum Design) magnetometer.

3. Results and Discussion

3.1. Morphology and Composition. The Ge NWs were grown at 800 °C using the thermal vapor transport of Ge powder and $MnCl_2$ (or $CoCl_2$, $FeCl_2$) beads. The growth mechanism follows the vapor−liquid−solid (VLS) mechanism using the Au catalytic nanoparticles. The doping level was controlled by adjusting the evaporation temperature of the metal precursors. The SEM and TEM images of the undoped Ge NWs are displayed in the Supporting Information, Figure S1. The $Ge_{1-x}Mn_x$ NW samples were selectively synthesized with controlled Mn contents: $x = 0.05 \pm 0.02$, 0.1 ± 0.03, and 0.2 ± 0.05. Figure 1a shows the SEM image of the $Ge_{0.9}Mn_{0.1}$ NWs grown homogeneously on the substrates. Their average length is 20 μm. The TEM image reveals that the nanowires have a smooth surface and uniform outer diameter with an average value of 60 nm (Figure 1b). The oxide (GeO_x) amorphous outer layers (av thickness = 5 nm) usually sheath the nanowire core, forming a Ge/GeO_x core/shell nanocable structure (inset). The lattice-resolved TEM image for a selected nanowire (its larger-scaled TEM image is shown in the inset of Figure 1b) is displayed in Figure 1c. The (111) fringes, perpendicular to the wire axis, are separated by a distance of about 3.2 Å, which is close to that of face-centered cubic Ge crystal ($a = 5.6576$ Å; JCPDS card no. 04-0545). The fast Fourier-transformed electron diffraction (FFT ED) pattern, at the [011] zone axis, confirms that the single-crystalline Ge nanocrystal grew in the [111] direction (inset). EDX elemental mapping reveals that the nanowires are homogeneously composed of Ge and Mn (Figure 1d). The scanning TEM (STEM) image is shown on the left. The average Mn content is 0.1 ± 0.03. We also synthesized $Ge_{0.95}Mn_{0.05}$ and $Ge_{0.8}Mn_{0.2}$ NWs having a similar morphology to that of the $Ge_{0.9}Mn_{0.1}$ NWs. The SEM image reveals the $Ge_{0.8}Mn_{0.2}$ NWs were grown homogeneously on the substrates (Figure 1e). The STEM image and its EDX mapping for a selected nanowire are shown in Figure 1f. The Mn element is distributed homogenously over the whole nanowire with an average Mn content of 0.2 ± 0.05. The EDX data of an individual nanowire are shown in the Supporting Information, Figure S2. The average value was obtained from the EDX measurement of 3−5 nanowires.

Figure 2a corresponds to the SEM image of the $Ge_{0.9}Fe_{0.1}$ NWs grown on the substrates. The TEM image reveals the Ge/GeO_x core/shell nanocable structure (Figure 2b and inset). The diameter of the nanowire core is about 40 nm, and the outer diameter of the nanocables is about 60 nm. Figure 2c shows the lattice-resolved TEM image of a selected Ge NW (its larger-scaled TEM image is in the inset of Figure 2b). The selected-area ED (SAED) pattern, measured at the [011] zone axis, further confirms the formation of single-crystalline Ge nanocrystals, grown along the [111] growth direction (inset). The (111) fringes are separated by a distance of about 3.2 Å. The EDX elemental mapping reveals the homogeneous distribution of $10\% \pm 3\%$ Fe over the whole Ge NW (Figure 2d). The left image shows the corresponding STEM image. We also synthesized $Ge_{0.9}Co_{0.1}$ NWs and observed that their morphology is similar to that of the other nanowires. Figure 2e displays their SEM image. The STEM image and EDX elemental mapping reveal that the nanowire consists of Ge and Co components (Figure 2f). The average Co content is 0.1 ± 0.03. Figure 2g corresponds to the TEM image of the $Ge_{0.6}Co_{0.4}$ NWs with a diameter of 70 nm. The STEM image and EDX elemental mapping reveal that the Co element is distributed over whole nanowire with an average content of 0.4 ± 0.1 (Figure 2h). The EDX data of these Fe- and Co-substituted Ge NWs are also shown in the Supporting Information, Figure S2.

3.2. XRD. The XRD pattern of the nanowire samples is displayed in Figure 3a. For comparison, the data of the Ge powder (purity 99.98%) was also measured. The peak positions of all of the samples exactly match with that of cubic Ge (*Fd*3*m*, $a = 5.6576$ Å; JCPDS card no. 04-0545). We carefully searched for secondary phases, but none were

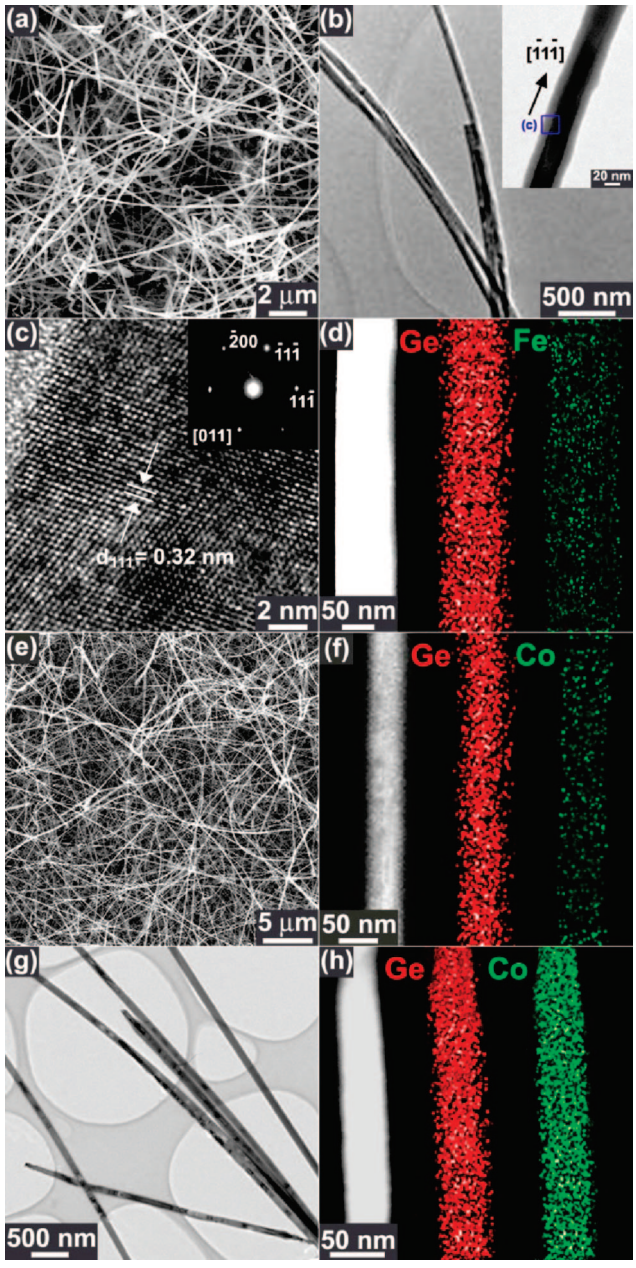

Figure 2. (a) SEM images of the $Ge_{0.9}Fe_{0.1}$ NWs grown on the substrates. (b) The TEM image shows their general morphology. The average diameter is 60 nm and the amorphous oxide layers sheath the nanowire core. (c) Lattice-resolved TEM images of a selected nanowire (its larger-scaled TEM image is shown in the inset of (b)) and its corresponding SAED pattern (inset), revealing the single-crystalline Ge nanocrystals grown along the [111] direction. (d) EDX elemental mapping shows the homogeneous Fe incorporation over the whole nanowire. The STEM image is shown on the left. (e) SEM images of the $Ge_{0.9}Co_{0.1}$ NWs grown on the substrates. (f) STEM image and EDX elemental mapping shows the homogeneous distribution of Co element over the whole nanowire. (g) TEM images of the $Ge_{0.6}Co_{0.4}$ NWs grown on the substrates. (h) STEM image and EDX elemental mapping show the homogeneous distribution of 40% Co over the whole nanowire.

observable, even in the logarithmically scaled XRD patterns. All of the $Ge_{1-x}M_x$ NWs have a highly crystalline structure without the formation of secondary phases. Figure 3b shows the magnified (111) peaks which serve to scrutinize the peak shift and broadening. The Mn-substituted Ge NWs exhibit a higher-angle shift; $\Delta(2\theta) = 0°$, 0.035°, and 0.020°, respectively, for $x = 0.05$, 0.1, and 0.2. As the Mn content increases to 0.1, the (111) peak shifts to a higher angle, but

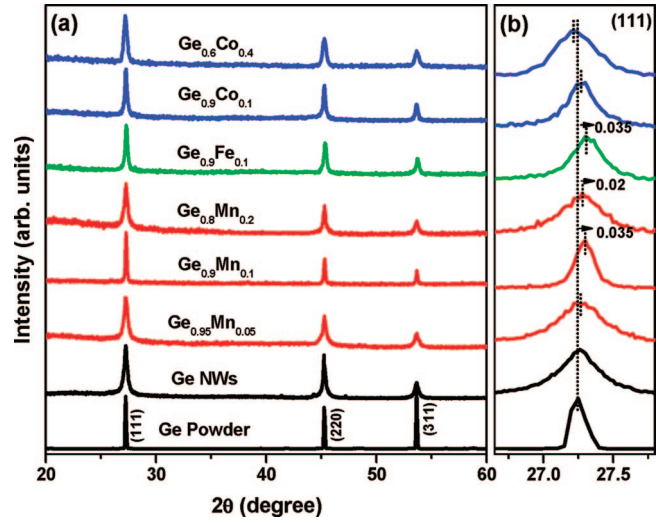

Figure 3. (a) XRD pattern of the Ge powder, Ge, $Ge_{0.95}Mn_{0.05}$, $Ge_{0.9}Mn_{0.1}$, $Ge_{0.8}Fe_{0.2}$, $Ge_{0.9}Fe_{0.1}$, $Ge_{0.9}Co_{0.1}$, and $Ge_{0.6}Co_{0.4}$ NWs. (b) The magnified (111) peak to show the peak shift and broadening.

this higher-angle shift decreases again with $x = 0.2$. The $Ge_{0.9}Fe_{0.1}$ NWs show a higher-angle peak shift of 0.035°, whereas the $Ge_{0.9}Co_{0.1}$ NWs show almost no shift. As the Co content increases to $x = 0.4$, the peak shifts slightly to a lower angle and becomes broader in width. The larger peak broadening of the nanowires, compared to that of the powder, indicates that there is more significant lattice distortion at the surface, probably due to their reduced crystal size. It is noticed that the $Ge_{0.9}Mn_{0.1}$ NWs exhibit a minimized lattice distortion.

The change in the lattice constants was estimated from the shift of (111) peak, as listed in Table 1, indicating that the Mn and Fe substitution induces a decrease of the lattice constant, whereas the Co substitution does not. It is predicted that the substitution of the covalent Ge ($r = 122$ pm) with the metal (covalent radius; $r_{Mn} = 127$ pm; $r_{Fe} = 124$ pm; $r_{Co} = 120$ pm) can expand the lattice constant for Mn and Fe.[8b,24] But the result is inconsistent with this prediction. As shown in section 3.5, we found Mn^{2+} and Fe^{2+} ions occupying the T_d sites using the XMCD data. Therefore, it is certainly difficult to explain the lattice constant change using the covalent radius. Nevertheless, the Mn-substituted Ge NWs definitely exhibit a decreasing-to-increasing behavior with a minimum at $x = 0.1$. Similar decreasing-to-increasing behavior of the lattice constant was observed for the epitaxially grown $Ga_{1-x}Mn_xN$ ($x \leq 0.09$) thin films, which showed an increase in the lattice constant above $x = \sim 0.03$.[25] The authors of this report suggested that the maximum value of the magnetization occurs at the minimized lattice constant, for the sample containing ~3% Mn. Recently, our group reported that the lattice constant (c) of room-temperature ferromagnetic $Ga_{1-x}Mn_xN$ NWs decreases initially and then increases as x increases above 0.03, which is coupled with their maximized magnetization.[26]

(24) Iwanowski, R. J.; Lawniczak-Jabłońska, K.; Golacki, Z.; Traverse, A. *Chem. Phys. Lett.* **1998**, *283*, 313.
(25) Thaler, G.; Frazier, R.; Gila, B.; Stapleton, J.; Davidson, M.; Abernathy, C. R.; Pearton, S. J.; Segre, C. *Appl. Phys. Lett.* **2004**, *84*, 1314.
(26) Hwang, S. O.; Kim, H. S.; Park, S.-H.; Park, J.; Bae, S. Y.; Kim, B.; Park, J. Y.; Lee, G. *J. Phys. Chem. C* **2008**, *112*, 2934.

Table 1. Change of the Lattice Constant of the $Ge_{1-x}M_x$ NWs, Raman Shift, XPS Ge 3d Peak Position/Width, XMCD L_3 Peak Intensity, and M_r and H_C of the Ge NWs and $Ge_{1-x}M_x$ NWs

					XPS Ge 3d peak (eV)				
no.	dopant (M)	x_M	lattice constant change Δa (Å)	Raman peak (cm^{-1})	position	width	XMCD intensity[a]	M_r (emu/g)[b]	H_C (Oe)[c]
1		0		299.2	32.6	1.6		0.003	50
2	Mn	0.05	~0	299.2 (0)[e]	32.2 (−0.4)[f]	1.6	7.5	0.01	50
3	Mn	0.1	−0.0068 (−0.12)[d]	299.8 (+0.6)	32.6 (0)	3.3	7.9	0.2	100
4	Mn	0.2	−0.0041 (−0.072)	299.2 (0)	32.3 (−0.3)	1.9	5.7	0.05	80
5	Fe	0.1	−0.0068 (−0.12)	299.4 (+0.2)	32.7 (−0.3)	3.0	1.1	0.002	50
6	Co	0.1	~0	298.6 (−0.6)	32.5 (−0.1)	1.6	~0	0.001	50
7	Co	0.4	~0	297.2 (−2.0)	32.5 (−0.1)	1.9	0.5	0.002	50

[a] The intensity of the XMCD L_3 peak of metal ions (2+) at 80 K in arbitrary units. [b] Remanence at 5 K in units of emu/g. [c] Coercive field at 5 K in units of Oe. [d] The parentheses correspond to the percentage reduction ("−" sign) relative to the lattice constant of the Ge NWs. [e] The value in the parenthesis represents the frequency shift (cm^{-1}) of the Ge−Ge phonon mode, relative to that of the Ge NWs. The "+" and "−" signs mean the higher- and lower-frequency shift, respectively. [f] The value in the parenthesis represents the shift of the 3d peak position, relative to that of the Ge NWs. The "−" sign means the lower-energy shift.

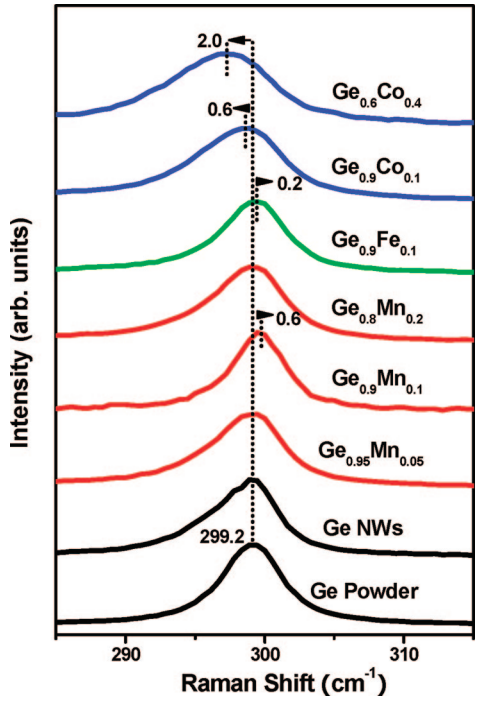

Figure 4. Raman spectra of the Ge powder, Ge, $Ge_{0.95}Mn_{0.05}$, $Ge_{0.9}Mn_{0.1}$, $Ge_{0.8}Fe_{0.2}$, $Ge_{0.9}Fe_{0.1}$, $Ge_{0.9}Co_{0.1}$, and $Ge_{0.6}Co_{0.4}$ NWs. The excitation wavelength is 514.5 nm from an argon ion laser.

From the present $Ge_{1-x}Mn_x$ ($x = 0.05$, 0.1, and 0.2) NWs, we observed that the minimum value of the lattice constant (with the minimized lattice distortion) occurs at $x = 0.1$. This result can be notably correlated with the maximized magnetic moment, as described in the following sections (sections 3.5 and 3.6). Furthermore, this reduced lattice constant would be ascribed to the hybridization between the dopants and host defects, as discussed in section 3.4. The absence of the lattice constant decrease for the $Ge_{0.9}Co_{0.1}$ and $Ge_{0.6}Co_{0.4}$ NWs is also well-correlated with their lack of magnetization and hybridization.

3.3. Raman Spectroscopy. Figure 4 displays the first-order Raman scattering spectra of the $Ge_{1-x}M_x$ NWs, and Table 1 lists the peak positions. The excitation wavelength is the 514.5 nm line of an argon ion laser. The appearance of the Ge−Ge phonon mode at ~299 cm^{-1} indicates that all of the NWs consisted of crystalline Ge. It was reported that for the Ge nanocrystalline film the spectral position and shape of this mode are very sensitive to the compressive strain at the interface with the Si substrates.[27] The spectra show peaks at 299.2, 299.2, 299.8, and 299.2 cm^{-1}, for the Ge, $Ge_{0.95}Mn_{0.05}$, $Ge_{0.9}Mn_{0.1}$, and $Ge_{0.8}Mn_{0.2}$ NWs, respectively. The higher-frequency shift (0.6 cm^{-1}) and the narrower bandwidth of $Ge_{0.9}Mn_{0.1}$ NWs would be directly related to the decrease of the lattice constant, as determined from the XRD peaks. The peak of the $Ge_{0.9}Fe_{0.1}$ NWs also appears at a higher frequency of 299.4 cm^{-1} (with a shift of 0.2 cm^{-1}). However, the $Ge_{0.9}Co_{0.1}$ and $Ge_{0.6}Co_{0.4}$ NWs show shifts to lower frequencies (298.6 and 297.2 cm^{-1}), respectively, corresponding to the shift of 0.6 and 2.0 cm^{-1}, and significant peak broadening, which could be related with their serious lattice distortion. All of these results are quite consistent with the change of the lattice constants determined from the XRD peaks.

3.4. XPS. The XPS survey scans of all of the samples show the Ge and metal peaks (Supporting Information, Figure S3). Figure 5a shows the fine-scanned Ge 3d peaks of all of the $Ge_{1-x}M_x$ NWs. Due to the thick GeO_x shell layers, the main peak at ~32.5 eV can be assigned mainly to Ge−O bonding structures, whereas the small peak at ~29 eV originated from Ge−Ge bonding structures. For these assignments, the XPS peak of the Ge powder is plotted. It is noteworthy that as the content of metal dopants increases, the Ge−O peak becomes broader in width and more asymmetric in the lower-energy region. The binding energy of the Ge bonded to the metal would be expected to appear at a lower energy compared to that of the Ge atoms bonded directly to the O atoms, based on the Pauling's electronegativity (χ_P) differences between Ge ($\chi_P = 2.01$), Mn ($\chi_P = 1.55$), Fe ($\chi_P = 1.83$), Co ($\chi_P = 1.88$), and O ($\chi_P = 3.44$).

The present XPS results show that the Ge−O peak shifts of the $Ge_{1-x}Mn_x$ NWs are −0.4, 0, and −0.3 eV (negative sign means the lower-energy shift), relative to the Ge NWs, for $x = 0.05$, 0.1, and 0.2, respectively, indicating nonlinear dependence on the Mn content. For the $x = 0.1$ Mn, Fe, and Co substitution, the peak shifts are 0, −0.3, and −0.1 eV, respectively, showing a lower-energy shift for the Fe and Co substitution. The $x = 0.4$ Co substitution does not induce further lower-energy peak shifts. The peak broadening of the $Ge_{1-x}Mn_x$ NWs is most significant with $x = 0.1$; the corresponding full width at half-maximums (fwhms) are 1.6,

(27) Cojocaru, C. V.; Bernardi, A.; Reparaz, J. S.; Alonso, M. I.; Macleod, J. M.; Harnagea, C.; Rosei, F. *Appl. Phys. Lett.* **2007**, *91*, 113112.

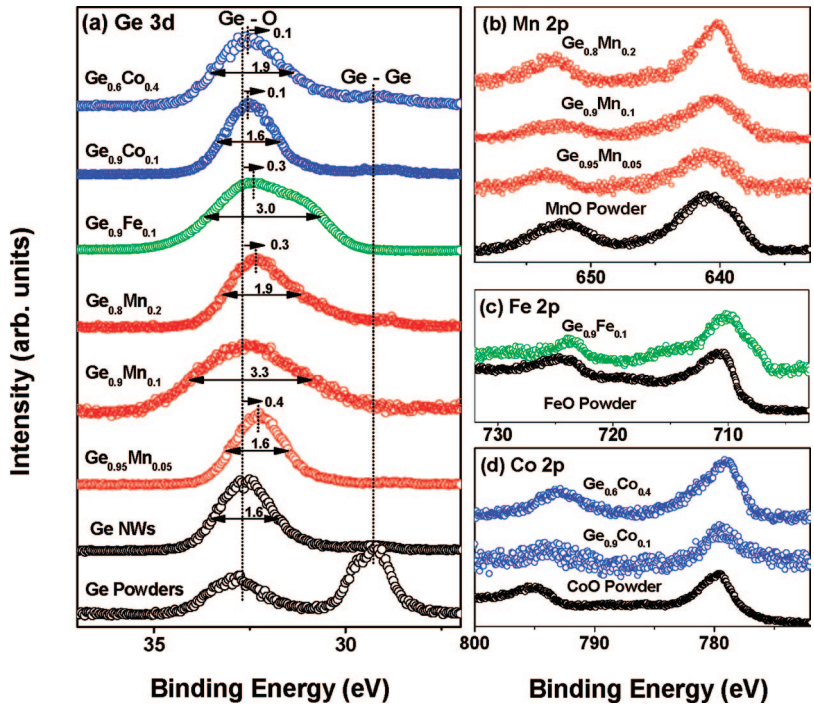

Figure 5. (a) Fine-scanned XPS Ge 3d peak of the Ge powder, undoped Ge, $Ge_{0.95}Mn_{0.05}$, $Ge_{0.9}Mn_{0.1}$, $Ge_{0.8}Mn_{0.2}$, $Ge_{0.9}Fe_{0.1}$, $Ge_{0.9}Co_{0.1}$, and $Ge_{0.6}Co_{0.4}$ NWs. (b) Fine-scanned XPS Mn $2p_{3/2}$ and $2p_{1/2}$ peaks of $Ge_{0.95}Mn_{0.05}$, $Ge_{0.9}Mn_{0.1}$, $Ge_{0.8}Mn_{0.2}$ NWs, and MnO powder. (c) Finely scanned XPS Fe $2p_{3/2}$ and $2p_{1/2}$ peaks of $Ge_{0.9}Fe_{0.1}$ NWs and FeO powder. (d) Finely scanned XPS Co $2p_{3/2}$ and $2p_{1/2}$ peaks of $Ge_{0.9}Co_{0.1}$, $Ge_{0.6}Co_{0.4}$ NWs, and CoO powder.

3.3, and 1.9 eV for Mn $x = 0.05$, 0.1, and 0.2, respectively. Among the $Ge_{0.9}Mn_{0.1}$, $Ge_{0.9}Fe_{0.1}$, and $Ge_{0.9}Co_{0.1}$ NWs, the peak broadening is insignificant only for Co substitution; fwhm = 3.3, 3.0, and 1.6 eV, respectively. The higher Co content ($x = 0.4$) increases the fwhm to 1.9 eV. The peak positions and fwhms are listed in Table 1. The Ge 2p and 3d peaks exhibit the same change of the peak shape and position for the metal substitution. Parts b−d of Figure 5 correspond to the finely scanned Mn, Co, and Fe 2p peaks, respectively. The peaks were compared with those of the MnO, FeO, and CoO powders, respectively. All of the peaks appear in a lower-energy region than these reference peaks, indicating that the metal ions are not completely oxidized to the oxide form. Although the analysis of the Ge−O peak (and metal peaks) mainly provides information on the electronic structure of the amorphous GeO_x outer layers, it may be still important to catch an insight of the electronic structures of Ge NWs (at least into the interface region). In fact, we find an attractive connection between the peak position/broadening and the magnetization, as described below.

The present $Ge_{1-x}Mn_x$ NWs exhibit room-temperature ferromagnetic properties, as in the case of the previously reported ferromagnetic $Ge_{1-x}Mn_x$ NWs, and this will be discussed below (sections 3.5 and 3.6).[21] For the room-temperature ferromagnetic Co-doped ZnO ($Zn_{1-x}Co_xO$, $x =$ 0.020, 0.056, and 0.098) nanoparticles reported by Wang et al., there was a strong correlation between the XPS peak position and the saturation magnetization.[28] The shift of the Zn 2p core-level to a high-energy region was maximized for $x = 0.056$, showing the same trend as the saturation magnetization. The authors suggested the existence of a strong hybridization between the dopant and defect wave functions, which is responsible for the higher-binding energy shift. They suggested that, for the highest doping concentrations, the energy of the partial Co ions (d levels) moves down to the O 2p band, thus lowering the probability for the overall overlap and scaling down the ferromagnetic signal. For the room-temperature ferromagnetic $Zn_{1-x}Mn_xO$ ($x = 0.05$, 0.1, and 0.2) NWs, our group reported that as the Mn content increases, the peak position shifts to the higher-energy region: 0.4 eV for $x = 0.05$, 0.7 eV for $x = 0.1$, and 0 eV for $x =$ 0.2, showing a maximum at $x = 0.1$.[29] The highest magnetization at $x = 0.1$ was correlated with the XPS peak shift. More recently, for the $Ga_{1-x}Mn_xN$ ($x = 0.01$, 0.02, 0.03, and 0.05) NWs, we observed the peak shift of Ga 2p to the higher-energy region: 0.4 eV for $x = 0.05$, 0.5 eV for $x = 0.02$, and 0.2 eV for $x = 0.03$ and 0.05, showing a maximum at $x = 0.03$, where the magnetization reaches a maximum.[26]

For these $Ge_{1-x}Mn_x$ NWs, we also proposed that the hybridization between the Mn dopant and the defects would lead a shift to the higher-binding energy. As regards the origin of the ferromagnetism, Kittilstved et al. suggested that, in p-type Mn-doped ZnO, there exists a shallow acceptor's hole-transfer process onto Mn^{2+} to form Mn^{3+}. This hole-transfer process can be described as $Mn^{2+} + h^+$ (acceptor) $\rightarrow Mn^{3+}$.[30] This dopant−acceptor hybridization is the pivotal feature determining the value of T_C in theoretical models describing DMS ferromagnetism. The same authors claimed

(28) Wang, X.; Xu, J.; Zhang, B.; Yu, H.; Wang, J.; Zhang, X.; Yu, J.; Li, Q. *Adv. Mater.* **2006**, *18*, 2476.

(29) Kang, Y. J.; Kim, D. S.; Lee, S. H.; Park, J.; Chang, J.; Moon, J. Y.; Lee, G.; Yoon, J.; Jo, Y.; Jung, M.-H. *J. Phys. Chem. C* **2007**, *111*, 14956.

(30) Kittilstved, K. R.; Liu, W. K.; Gamelin, D. R. *Nat. Mater.* **2006**, *5*, 291.

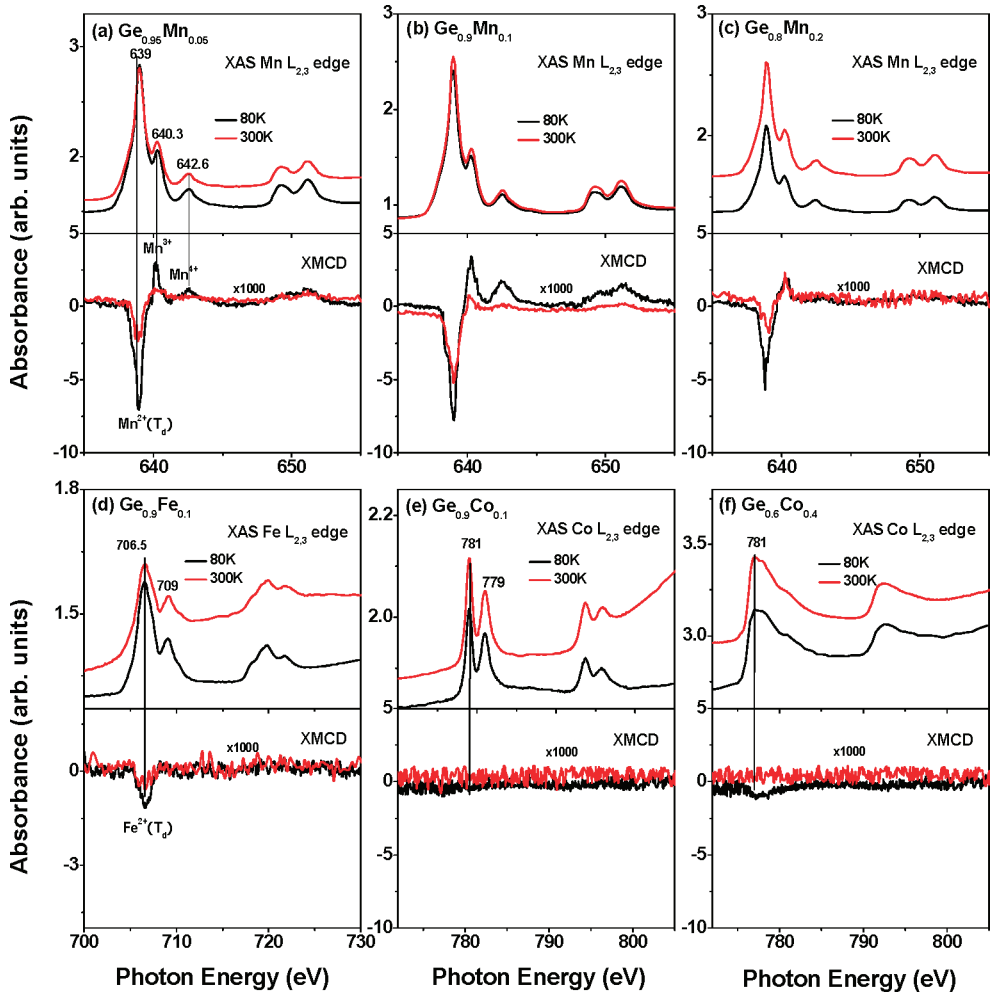

Figure 6. XAS and XMCD spectra of the Mn $L_{2,3}$ edge region for the (a) $Ge_{0.95}Mn_{0.05}$, (b) $Ge_{0.9}Mn_{0.1}$, (c) $Ge_{0.8}Mn_{0.2}$ NWs; Fe $L_{2,3}$ edge region for the (d) $Ge_{0.9}Fe_{0.1}$ NWs; Co $L_{2,3}$ edge region for the (e) $Ge_{0.9}Co_{0.1}$ and (f) $Ge_{0.6}Co_{0.4}$ NWs, measured at 80 and 300 K.

that there is no ferromagnetism in p-type Co-doped ZnO, since the hybridization of Co^{2+} ions with holes is not allowed. This type of hybridization may occur in the present Mn- and Co-substituted Ge NWs, which presumably contain p-type defects (i.e., Ge vacancies).

The incorporation of the less electronegative Mn (compared to Ge) would cause the initial lower-energy shift of the Ge 3d peaks. However, as the Mn content increases from $x = 0.05$ to 0.1, the peak moves to a higher energy, which can be rationalized by the hybridization. However, as the Mn content increases from $x = 0.1$ to 0.2, the peak moves to a lower energy, which can be explained by the reduced hybridization. The XRD data shows a minimum value of the lattice constant at $x = 0.1$, which would be directly related to the fact that the maximum hybridization takes place. For the Fe-doped Ge NWs, there may be a chance for dopant−acceptor hybridization involving the hole-transfer process $Fe^{2+} + h^+$ (acceptor) → Fe^{3+} to occur, since the lattice constant decreases (as evidenced by XRD and Raman spectroscopy). However, the lower-energy shift of the $Ge_{0.9}Fe_{0.1}$ NWs suggests the presence of insufficient hybridization at this Fe content. In order to confirm this tentative conclusion, we need more data regarding the dependence on the Fe content. The absence of a higher-energy shift for the $Ge_{0.9}Co_{0.1}$ and $Ge_{0.9}Co_{0.1}$ NWs is directly related to the absence of hybridization ($Co^{2+} + h^+$ (acceptor) → Co^{3+}), which is supported by no decrease of the lattice constant (as shown in section 3.2). These results are also consistently predicted by ab initio calculations on the doping of a series of first-period transition metals in the Ge matrix, for which Mn doping is the most efficient in forming ferromagnetism.[19]

3.5. XAS and XMCD. In order to further investigate the electronic structure of the Mn ions, we performed XAS and XMCD ($\Delta\rho = \rho^+ - \rho^-$) measurements at the Mn $L_{2,3}$ edges. The degree of circular polarization of the incident light is expected to be 95%. Figure 6a−c, shows the Mn $L_{2,3}$ edge XAS and XMCD spectra of the $Ge_{0.95}Mn_{0.05}$, $Ge_{0.9}Mn_{0.1}$, and $Ge_{0.8}Mn_{0.2}$ NWs, respectively, measured at 80 and 300 K. The spectra, which result from the Mn 2p → 3d dipole transition, are divided roughly into the L_3 ($2p_{3/2}$) and L_2 ($2p_{1/2}$) regions. The absorption intensity increases as the temperature decreases to 80 K. The multiplet absorption feature and the peak position (639−642.6 eV) suggest that the Mn dopant is in a bonding state, not in a metallic state such as Mn clusters.[31] The lower figure corresponds to the XMCD spectra. The main negative signal of the L_3 peak at 639.0 eV can be observed, which indicates the contribution

(31) Grabis, J.; Bergmann, A.; Nefedov, A.; Westerholt, K.; Zabel, H. *Phys. Rev. B* **2005**, *72*, 024437.

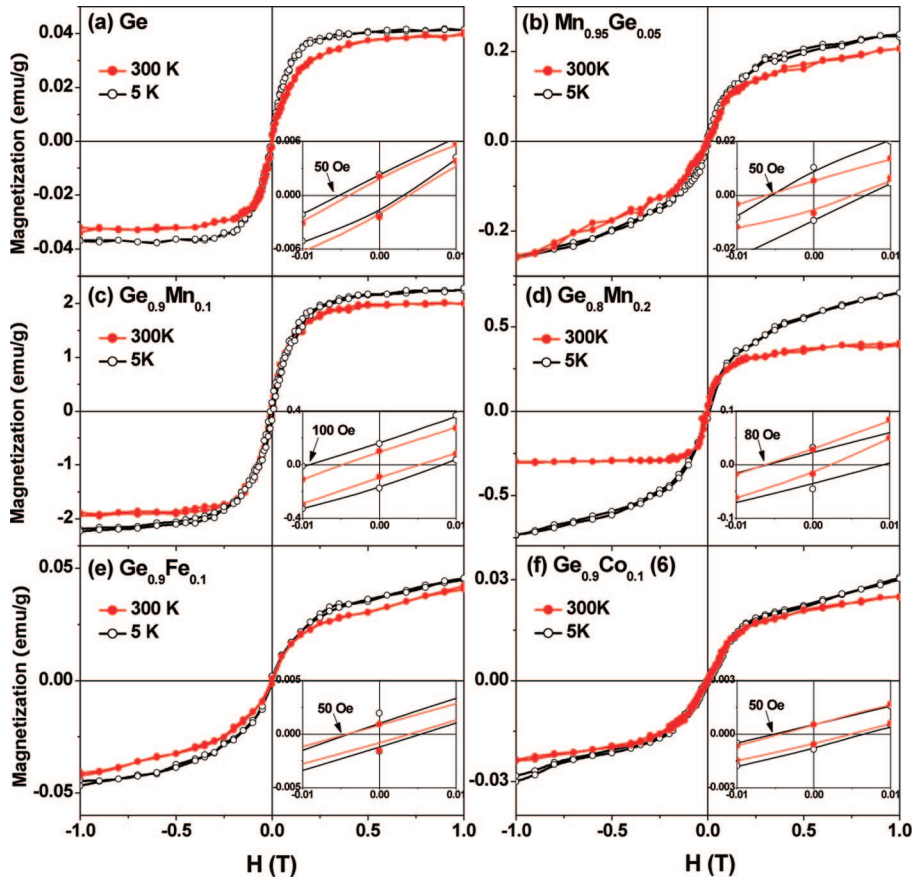

Figure 7. Field-dependent magnetic moment ($M-H$) curves for (a) Ge, (b) $Ge_{0.95}Mn_{0.05}$, (c) $Ge_{0.9}Mn_{0.1}$, (d) $Ge_{0.8}Mn_{0.2}$, (e) $Ge_{0.9}Fe_{0.1}$, and (f) $Ge_{0.9}Co_{0.1}$ NWs, measured at 5 and 300 K.

of Mn^{2+} at the T_d sites, substituting for the Ge.[31,32] These Mn^{2+} ions would be responsible for the ferromagnetism of the Ge NWs (section 3.6). The positive signals at 640.3 and 642.6 eV can be assigned to Mn^{3+} and Mn^{4+} ions, respectively. As the Mn content increases from $x = 0.05$ to $x = 0.1$, the intensity of the XMCD increases. However, when the Mn content reaches $x = 0.2$, the intensity deceases. The intensity of the negative L_3 Mn^{2+} peak (at 80 K) is listed in Table 1, indicating that the magnetic moment of the Mn^{2+} ions reaches a maximum when $x = 0.1$. This result is consistent with the XRD and XPS data showing that the Mn substitution with $x = 0.1$ is most effective in increasing the dopant−acceptor hybridization. The presence of Mn^{3+} ions may provide evidence for such hybridization involving the hole-transfer process.

Figure 6d shows the Fe $L_{2,3}$ edge XAS and XMCD spectra of the $Ge_{0.9}Fe_{0.1}$ NWs, measured at 80 and 300 K. The split absorption feature and the position (at 706.5 eV) suggest that the Fe^{2+} ions are in a bonding state, not metallic Fe. The lower figure corresponds to the XMCD spectra, showing a low-intensity negative signal of the L_3 peak for both temperatures. This indicates the contribution of the Fe^{2+} ions at the T_d sites, substituting for Ge. Parts e and f of Figure 6 show the Co $L_{2,3}$ edge XAS and XMCD spectra of the $Ge_{0.9}Co_{0.1}$ and $Ge_{0.6}Co_{0.4}$ NWs, respectively, measured at 80 and 300 K. The shape of the $Ge_{0.9}Co_{0.1}$ NWs is similar to that of the Co ions in the bonding states; multiplet structures (like Mn and Fe) are present.[31,32] However, the $Ge_{0.6}Co_{0.4}$ NWs show a typical metallic feature without a split peak, suggesting that the higher Co doping may induce the formation of Co metal clusters, which XRD or Raman spectroscopy cannot detect. The lower figure corresponds to the XMCD spectrum, showing no magnetic moments for either sample. This absence of a magnetic moment is consistent with the XPS data described above.

3.6. Magnetic Moment Measurement Using SQUID. The magnetic moment (M) versus magnetic field (H) curves at 5 and 300 K were measured by the SQUID magnetometer. The nanowires were separated from the substrates. Figure 7a corresponds to the field-dependent $M-H$ curve of the undoped Ge NWs. Hysteresis occurs with a saturation field of ~0.3 T at both temperatures. The inset displays the curve in the vicinity of $H = 0$, indicating that the coercive field (H_C) is 50 Oe and the remanence (M_r) is 0.003 emu/g at 5 K. Therefore, the existence of ferromagnetism at 5 and 300 K is clearly proven by the coercivity and remanence, and relatively low saturation field, suggesting that the T_C value is at least 300 K. The field-cooled (FC) and zero-field-cooled (ZFC) magnetic moment versus temperature (M_{FC} and M_{ZFC} vs T) curves with $H = 100$ Oe are displayed in the Supporting Information, Figure S4, indicating $T_C > 350$ K.

Figure 7b−d, displays the $M-H$ curves of the $Ge_{0.95}Mn_{0.05}$, $Ge_{0.9}Mn_{0.1}$, and $Ge_{0.8}Mn_{0.2}$ NWs, respectively, consistently showing hysteresis at 5 and 300 K. The hysteresis curves

(32) Miyamoto, K.; Iori, K.; Kimura, A.; Xie, T.; Taniguchi, M.; Qiao, S.; Tsuchiya, K. *Solid State Commun.* **2003**, *128*, 163.

show that $M_r = 0.01$, 0.2, and 0.05 emu/g and $H_C = 50$, 100, and 80 Oe, for $x = 0.05$, 0.1, and 0.2, respectively, at 5 K (inset). The values of M_r and H_C are summarized in Table 1. As the Mn content increases from $x = 0.05$ to $x = 0.1$, the M_r increases by a factor of ~20. As it increases further to $x = 0.2$, the M_r decreases by a factor of ~4. This result indicates that the magnetic moment reaches a maximum for $x = 0.1$. The M_{FC} and M_{ZFC} versus T curves are displayed in the Supporting Information, Figure S4, indicating $T_C > 350$ K.

Figure 7e corresponds to the $M-H$ curves of the $Ge_{0.9}Fe_{0.1}$ NWs, showing hysteresis at 5 and 300 K. Figure 7f displays the hysteresis curves of the $Ge_{0.9}Co_{0.1}$ NWs at 5 and 300 K. The ferromagnetism can be clearly seen from these samples. The insets indicate that $H_C = 50$ Oe and $M_r = 0.001$ and 0.002 emu/g at 5 K, respectively, for the $Ge_{0.9}Fe_{0.1}$ and $Ge_{0.9}Co_{0.1}$ NWs. The $M-H$ curve of the $Ge_{0.6}Co_{0.4}$ NWs are very similar to those of the $Ge_{0.9}Fe_{0.1}$ NWs (not shown here), indicating that the higher Co content does not enhance the magnetic moment. The M_{FC} and M_{ZFC} versus T curves are displayed in the Supporting Information, Figure S4, indicating $T_C > 350$ K.

The ferromagnetic behaviors of undoped Ge NWs are quite surprising. Recently, however, the size-dependent ferromagnetism of Ge nanoparticles (deposited on polystyrene or Si substrates) has been reported.[33] The authors suggested that this was due to the occurrence of the quantum confinement effect owing to their large Bohr radius (~17 nm). For the magnetism of the nanocrystalline forms, the mechanisms invoked so far are usually based on uncompensated spins and surface anisotropy, because of the high surface/volume ratio. These unusual ferromagnetic properties of the Ge NWs can probably be explained by the surface contribution. Further investigation is necessary to clearly explain the ferromagnetic properties of the Ge NWs. We are currently conducting experiments to examine the effect of the catalyst or substrates on the magnetic properties.

The magnetic moment of the $Ge_{1-x}Mn_x$ NWs overwhelms that of the undoped Ge and reaches a maximum with $x = 0.1$. This result is consistent with the XAS and XMCD data showing that the Mn substitution with $x = 0.1$ leads to the greatest increase in the magnetic moment of the Mn^{2+} ions. In the case of Fe or Co substitution, the magnitude of the magnetic moment is nearly the same as that of the undoped Ge NWs. The Co substitution does not lead to the enhancement of the ferromagnetism, due to the lack of hybridization. The Fe substitution may induce hybridization (as suggested by XRD and Raman spectroscopy), but 10% Fe substitution results in a much lower magnetic moment (or magnetization) than the Mn substitution. Therefore, we conclude that Mn substitution can be used to produce powerful ferromagnetic Ge NWs.

(33) (a) Liou, Y.; Su, P. W.; Shen, Y. L. *Appl. Phys. Lett.* **2007**, *90*, 182508. (b) Liou, Y.; Lee, M. S.; You, K. L. *Appl. Phys. Lett.* **2007**, *91*, 082505.

4. Conclusions

We synthesized Ge, $Ge_{0.95}Mn_{0.05}$, $Ge_{0.9}Mn_{0.1}$, $Ge_{0.8}Mn_{0.2}$, $Ge_{0.9}Fe_{0.1}$, $Ge_{0.9}Co_{0.1}$, and $Ge_{0.6}Co_{0.4}$ NWs, by the vapor transport of Ge and $MnCl_2$ (or $FeCl_2$, $CoCl_2$). Their average diameter is about 60 nm. They all consist of single-crystalline cubic Ge nanocrystals grown uniformly with the [111] direction, irrespective to the metal doping. All have amorphous GeO_x outer layers. The EDX data reveal that the metal dopes homogeneously over the entire nanowires. We investigated their electronic structures and magnetic properties by XRD, Raman spectroscopy, XPS, XAS, XMCD, and MPMS (magnetic property measurement system).

The XRD pattern shows no formation of metal clusters for any of the nanowires, and the decrease of the lattice constant in the case of Mn and Fe substitution, but not in the case of Co substitution. Raman spectroscopy supports this result. The XPS data shows a higher-energy shift of the Ge peak in the case of 10% Mn substitution. The Fe and Co substitution induces a lower-energy shift for all contents. The XAS and XMCD measurements reveal that the Mn^{2+} ions preferentially occupy the T_d sites, substituting for Ge, and their magnetic moment reaches a maximum at $x = 0.1$. The Fe ions also substitute for Ge at the T_d sites, but their magnetic moment is much smaller than that of the Mn ions. In contrast, the Co ions do not have any magnetic moment at all. The magnetic moment measurement using SQUID reveals that they all exhibit ferromagnetic behaviors at room temperature, even the undoped Ge NWs. The $Ge_{1-x}Mn_x$ NWs exhibit a much larger magnetic moment than the undoped Ge NWs and consistently exhibit a maximum value at $x = 0.1$. However, the Fe and Co substitutions do not lead to a significant increase in the ferromagnetism. On the basis of these results, we suggest the possibility of hybridization between the metal ions and host defects in p-type Ge, which could be a crucial feature in determining the ferromagnetism. We conclude that the Mn substitution is more effective to form ferromagnetic Ge NWs, compared to the Fe or Co substitution, which can be applicable to the fabrication of nanoscale spintronic devices.

Acknowledgment. This work was supported by KRF Grants (R14-2003-033-01003-0; R02-2004-000-10025-0; 2003-015-C00265), KOSEF (R01-2008-000-10825-0; 2008-02364), and BK21. The SEM, TEM (or HVEM), XRD, XPS, and SQUID measurements were performed at the Korea Basic Research Institute (Seoul, Daejeon, Taegu, and Pusan). The experiments at the PLS were supported in part by MOST and POSTECH.

Supporting Information Available: Additional TEM images, EDX, XPS survey scans, and MPMS data (PDF). This material is available free of charge via the Internet at http://pubs.acs.org.

CM7035635